Journal Name

ARTICLE TYPE

Cite this: DOI: 10.1039/xxxxxxxxxx

High-throughput electrical position detection of single flowing particles/cells with non-spherical shape†

Riccardo Reale,[a] Adele De Ninno,[a] Luca Businaro,[b] Paolo Bisegna,[a] and Federica Caselli*[a]

We present an innovative impedance cytometer for the measurement of the cross-sectional position of single particles or cells flowing in a microchannel. As predicted by numerical simulations and experimentally validated, the proposed approach is applicable to particles/cells with either spherical or non-spherical shape. In particular, the optics-free high-throughput position detection of individual flowing red blood cells (RBCs) is demonstrated and applied to monitor RBCs hydrodynamic focusing under different sheath flow conditions. Moreover, the device provides multiparametric information useful for lab-on-a-chip applications, including particle inter-arrival times and velocity profile, as well as RBCs mean corpuscular volume, distribution width and electrical opacity.

1 Introduction

Cell manipulation techniques combined with microfluidic technology play a critical role in various applications in cell biology, clinical research and biomedical engineering.[1] Microfluidic devices have been developed for applications such as cell focusing, alignment, trapping and separation of target cells from heterogeneous solutions, by exploiting geometric,[2,3] electric,[4–6] magnetic,[7] acoustic,[8] or mechanical[9,10] properties. Besides spherical objects manipulation, approaches suited to non-spherical particles and cells (e.g., red blood cells and bacteria) are of notable importance.[11] With respect to spherical particles, non-spherical ones may exhibit different behaviours of e.g. inertial focusing,[12–14] dielectrophoretic focusing,[15] impedance spectroscopy,[16,17] and deterministic lateral displacement.[11,18]

Currently, the efficiency of most manipulation devices is determined by analyzing the outlet samples (e.g., by hemocytometer[19] or FACS machine[8]) or by particle position detection inside the microdevice with optical means.[6,11,15] Conventional microscopy approaches provide two-dimensional images of either the device top view or side view, but they are not suited to visualize particle cross-sectional position. Moreover, they require transparent materials and demand for acquisition and processing of large image data sets. More advanced optical systems find limited application due to their setup complexity.[20–22] Hence there is a pressing need for simple and effective methods to characterize the motion of single particles at the microscale.[23–25]

An emerging alternative to optical systems for particle position detection is represented by electrical impedance-based approaches. Wang et al.[26] reported a system where a single pair of non-parallel microelectrodes was utilized to detect the lateral (i.e., along channel width) position of particles flowing in a microchannel. Brazey et al.[27] presented an impedance-based real-time sensor for the detection of the longitudinal (i.e., along channel length) position. Solsona et al.[28] exploited a gradient in the electric field to detect the position of particles in one axis. We recently presented a microfluidic impedance chip for the determination of both lateral and vertical (i.e., along channel height) position.[29] All those approaches were demonstrated for polystyrene beads.

In this work, we propose a novel microfluidic impedance chip for the position detection of particles/cells with non-spherical shape. As detailed in Section 2, the chip comprises two regions, one for the measurement of particle lateral position and one for the measurement of particle vertical position (Figure 1). Non-conventional wiring schemes are used to generate electric signals with enhanced information content.[30,31] They yield two metrics suitable to reconstruct particle position in the channel cross-section. In order to assess the robustness of those metrics with respect to particle volume, shape and orientation, a numerical study is performed. In particular, finite element (FEM) simulations of erythrocytes (i.e., discocytes) and prolate ellipsoids flowing through the microchannel with different orientations and cross-sectional positions are carried out (Section 4.1). Then, an experimental campaign is conducted and the optics-free

[a] Department of Civil Engineering and Computer Science, University of Rome Tor Vergata, 00133 Rome, Italy. E-mail: caselli@ing.uniroma2.it

[b] Institute for Photonics and Nanotechnologies, Italian National Research Council, 00156 Rome, Italy

† Electronic Supplementary Information (ESI) available. See DOI: 10.1039/xxxxxxxxxx

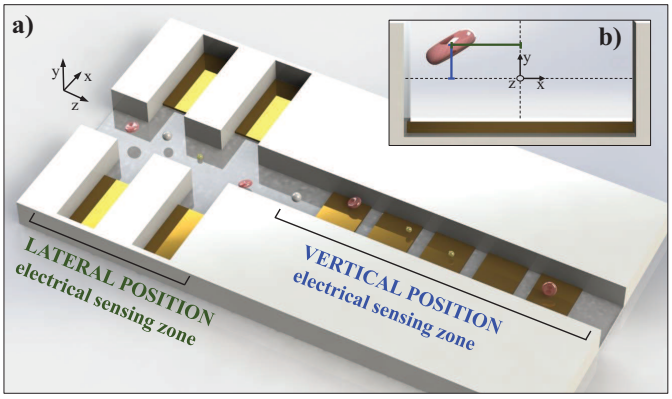

Fig. 1 Novel microfluidic impedance chip for cross-sectional position detection of flowing particles/cells. (a) 3D rendering of the device. The chip is formed by one region for the measurement of the lateral position (i.e., x-coordinate) and one for the measurement of the vertical position (i.e., y-coordinate). The former comprises two pairs of coplanar electrodes housed in side-channels, whereas the latter comprises five coplanar electrodes spanning the main channel width. (b) Schematic drawing of the cross-sectional position components of an individual flowing particle.

high-throughput cross-sectional position detection of individual flowing red blood cells is demonstrated for the first time (Section 4.2). As an application, the method is used to monitor the hydrodynamic focusing of erythrocytes and beads under different sheath flow conditions (Section 4.4). Finally, the capability of this simple device to provide multiparametric cell characterization is demonstrated (Section 4.5).

2 Operating principle

The region for the measurement of particle lateral position (i.e., x-coordinate) is equipped with two pairs of metal electrodes patterned at the bottom of dead-end lateral chambers (Figure 1). An AC voltage is applied to diagonally opposite stimulating electrodes housed in side channels, and the differential current I_Δ flowing through the remaining measuring electrodes is collected (Figure 2(a)). The resulting signal is a bipolar Gaussian with asymmetric peaks (Figure 2(c)). As demonstrated in our previous work,[31,32] the pulse amplitude difference, i.e. $a_2 - a_1$, conveys information on particle lateral position. In particular, it is positive if the particle flows in the $x > 0$ half of the channel (as in Figure 2(c)), whereas it is negative if the particle flows in the $x < 0$ half of the channel. In fact, the relative difference of pulse amplitudes (i.e., pulse amplitude difference divided by pulse amplitude average) is used to obtain a metric independent of particle size:

$$\Delta = \frac{a_2 - a_1}{(a_1 + a_2)/2}\,. \tag{1}$$

With respect to the approach used in Reale et al.[29] (cf. Figure S1), the present solution enables a significant reduction of the length of the lateral position sensing zone, in favour of device compactness, and requires only one current signal instead of two, thus easying acquisition and processing.

The region for the measurement of particle vertical position (i.e., y-coordinate) is equipped with five coplanar electrodes located on the bottom of the main channel and spanning the channel width (Figure 1). An AC voltage is applied to the third of the five electrodes in the main channel and the differential current I_P flowing through the first and the fifth electrodes is collected, the other two electrodes being floating (Figure 2(b)). The resulting signal trace exhibits a bipolar double-Gaussian profile (Figure 2(d)). As demonstrated in De Ninno et al.,[30] the prominence of the two peaks with respect to the saddle in between conveys information on particle vertical position. In particular, it is higher for particles traveling close to the electrodes (as in Figure 2(b)) than for particles traveling away from the electrodes. Because signal amplitude also depends on particle size, the following normalized metric, referred to as relative prominence, is used:

$$P = \frac{M - m}{M}\,, \tag{2}$$

where m and M correspond to the signal amplitude at the saddle and peaks, respectively.

It is noticed that in the lateral position determination region the electric field is nearly uniform across the channel height,[30] therefore the current I_Δ is practically independent from particle vertical position. Similarly, in the vertical position determination region the electric field is nearly uniform across the channel width,[31] therefore the current I_P is practically independent from particle lateral position.

A gallery of simulated signals relevant to a spherical particle travelling along z at different cross-sectional positions is shown in Figure S2. Taken together, the peak amplitude relative difference Δ and the relative prominence P provide information on particle cross-sectional position.

3 Materials and methods

3.1 Finite element simulations

The effect that deviation from spherical particle geometry might have on the proposed position detection strategy was investigated by FEM analysis. In particular, the differential current traces I_Δ and I_P generated by erythrocyte-shaped particles and prolate ellipsoids flowing through the microchannel with different orientations and cross-sectional positions were simulated. Model equations have been described elsewhere[33,34] and model dielectric parameters are reported in Table S1.

The shape of the erythrocyte was recreated using the axisymmetric parametric model described in San Martín et al.,[35] assuming parameters relevant to the normocyte (volume 85.1 μm^3). Simulations were performed for twenty-three different orientations of the erythrocyte axisymmetric axis, spanning the whole solid angle. An aspect ratio equal to two and a volume of 113.1 μm^3 were chosen for the prolate ellipsoid, and orientations along the three coordinate axes were considered.

For each orientation, fourteen cross-sectional positions of the flowing erythrocyte/ellispoid were considered. In particular, seven erythrocytes/ellipsoids with center at $y = 0$ and x-coordinate spanning the channel width were considered for I_Δ, whereas seven erythrocytes/ellipsoids with center at $x = 0$ and y-coordinate spanning the channel height were considered for

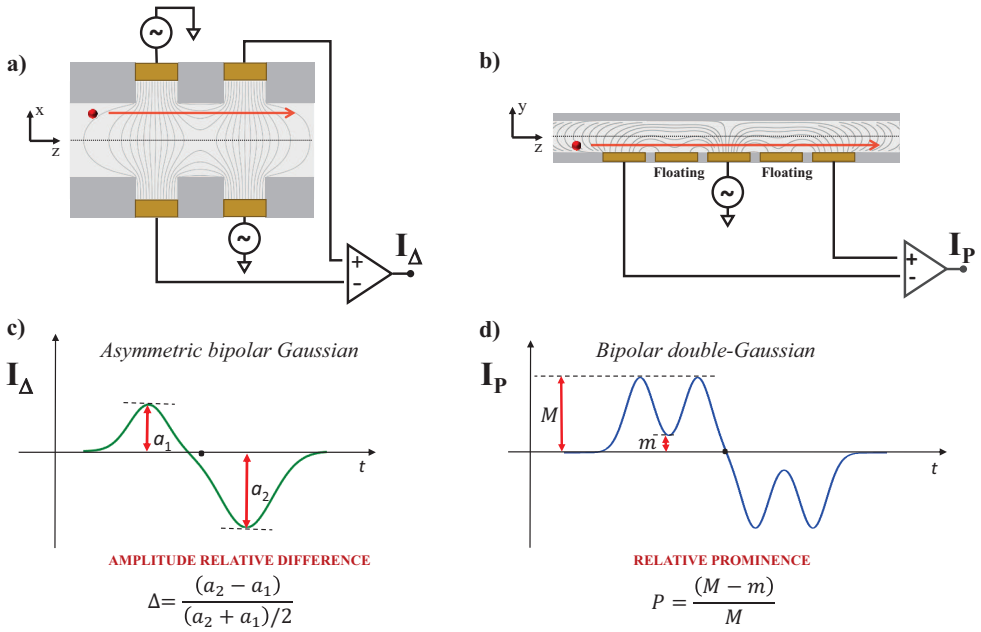

Fig. 2 Schematic drawing of the non-conventional electrode configurations used for position determination. (a) Particle lateral position (i.e., x-coordinate) is measured using a four-electrode configuration. The AC voltage is applied to two diagonally opposite electrodes and the differential current I_Δ flowing through the two remaining electrodes is collected. An asymmetric bipolar Gaussian template (c) is used to fit the differential current I_Δ, thus extracting the amplitudes a_1 and a_2, which in turn yield the amplitude relative difference Δ, correlating with particle lateral position. b) Particle vertical position (i.e., y-coordinate) is measured using a five-electrode configuration. The AC voltage is applied to the central electrode and the differential current I_P flowing through the first and last electrodes is collected. The second and fourth electrodes are left floating. A bipolar double Gaussian template (d) is used to fit the differential current I_P, thus extracting the amplitudes M and m, which in turn yield the relative prominence P, correlating with particle vertical position.

I_P. For comparison purposes, 7 μm spherical beads (volume 179.6 μm^3) were also analyzed in simulation.

From each trace, the relevant electrical metric was obtained (i.e., the amplitude relative difference Δ from I_Δ, and the relative prominence P from I_P) by fitting the appropriate template (i.e., the asymmetric bipolar Gaussian and the bipolar double-Gaussian, respectively, shown in Figure 2(c) and (d)).

3.2 Microfluidic chip

The microfluidic impedance chip used in the experimental campaign consists of a PDMS-embedded microchannel bonded to a glass microscope slide with integrated gold microelectrodes. Standard microfabrication techniques were used as reported elsewhere.[30] A microscopic image of the fluidic and electrode layouts is reported in Figure 3. The main channel was 50 μm wide and 21.5 μm high. The dead-end lateral chambers were 30 μm wide and 30 μm apart from each other, with electrodes recessed by 15 μm with respect to the main channel. The five electrodes spanning the main channel width were 30 μm wide with a 10 μm gap. Sheath flow channels were 40 μm wide and joined the main channel in a 20° junction 600 μm upstream the first measuring zone. It is noticed that sheath flows are not required for particle position detection. They are used in this work to show the ability of the device to monitor particle hydrodynamic focusing. Arrays of micro-pillars were included at each inlet fluidic port to reduce the risk of channel clogging.

3.3 Sample preparation

A 5 μl droplet of blood was obtained from a healthy donor by finger prick. The blood was diluted 1:10000 in a buffer formed by isotonic saline solution (0.90% w/v NaCl) with the addition of 150 mg/ml bovine serum albumin (BSA, Sigma-Aldrich) to increase solution density, and polystyrene beads (7 μm diameter, Sigma-Aldrich) at a concentration of about $2 \cdot 10^5$ beads/ml. The sheath flow buffer was formed by isotonic saline solution with the same concentration of dissolved BSA.

3.4 Fluidic setup

The sample flow rate, Q_{sa}, was supplied by a syringe pump (Elite 11, Harvard Apparatus, 500 μl Hamilton glass syringe). A pressure regulator (OB-1 Mk-3, Elveflow) was used to pressurize the sheath buffer reservoir. A flow sensor (MSF3, Elveflow) measuring the flow downstream the reservoir was used in a feedback loop to regulate the sheath flow rate, Q_{sh}. Teflon tubing were used for all liquid connections, whereas Tygon tubing were used for the air line.

Seven experiments were carried out: system calibration (denoted by C, cf. Section 3.7), optical validation (denoted by V, cf. Section 4.3), four experiments of hydrodynamic focusing (denoted by HF-1 to HF-4, cf. Section 4.4), and multiparametric analysis (denoted by M, cf. Section 4.5). In experiments C, V, M and HF-4 the sheath flow was split in a T-junction and connected to both sheath flow channels (virtually, $Q_{sh}^R = Q_{sh}^L = Q_{sh}/2$, where Q_{sh}^R and Q_{sh}^L denote right and left sheath flow rates, respectively,

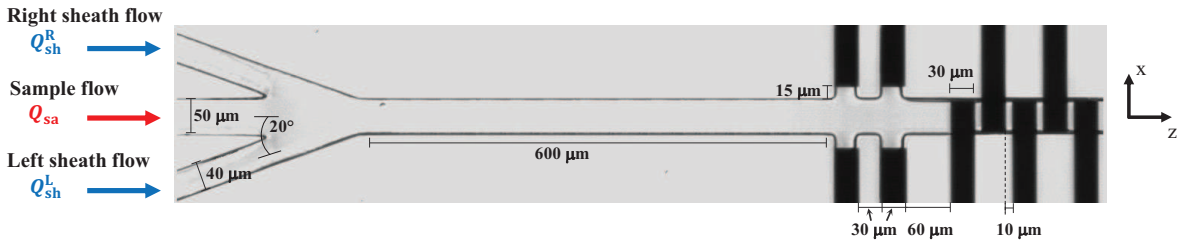

Fig. 3 Microscopic image showing the fluidic and electrode layouts.

Table 1 Experimental conditions used for system calibration (C), optical validation (V), multiparametric analysis (M), and hydrodynamic focusing (HF-1 to HF-4).

Exp.	Q_{sa} [µl/min]	Q_{sh}^{R} [µl/min]	Q_{sh}^{L} [µl/min]
C, V, M	15	2.5	2.5
HF-1	15	5	–
HF-2	10	10	–
HF-3	2	18	–
HF-4	2	9	9

cf. Figure 3). In experiments HF-1 to HF-3 the sheath flow source was connected to the right sheath flow channel only, the left one being blocked (accordingly, $Q_{sh}^{R} = Q_{sh}$ and $Q_{sh}^{L} = 0$). The flow rate values used in the experiments are reported in Table 1. In all cases, a total flow rate $(Q_{sh} + Q_{sa})$ of 20 µl/min was considered.

3.5 Electrical measurements

The differential currents I_Δ and I_P were measured using two transimpedance amplifiers (HF2TA, Zurich Instruments) and an impedance spectroscope (HF2IS, Zurich Instruments, working at 115 kSa/s sampling rate, 30 kHz filter bandwidth). An excitation signal of 8 V_p (peak) at 500 kHz was used in the lateral position sensing zone (i.e., for acquiring I_Δ), and an excitation signal of 4 V_p at 615 kHz was used in the vertical position sensing zone (i.e., for acquiring I_P). The selected frequencies (500 and 615 kHz) are below the range of the beta dispersion and differ by the sampling rate, thus reducing cross-talk effects. For multiparamteric analysis (experiment M in Table 1), the vertical position sensing zone was simultaneously stimulated with 4 V_p at 1 MHz, in order to compute an electrical opacity (cf. Section 4.5). The data streams were processed using an event detection algorithm,[36] and single-event features were extracted by template fitting using a custom MATLAB script. In particular, for each detected event the amplitude relative difference Δ (Eq. (1)) was computed from the peak amplitudes a_1 and a_2 of the asymmetric bipolar Gaussian template fitted to I_Δ, whereas the relative prominence P (Eq. (2)) was extracted from the bipolar double-Gaussian template fitted to I_P. The electrical volume (cf. Section 4.5) was used to distinguish between beads and erythrocytes and to plot the separate population data.

3.6 Optical measurements

A high-speed camera (Photron FASTCAM Mini UX100, 4000 fps, 4 μs shutter time) mounted on an inverted microscope (Zeiss Axio Observer, 20× objective) was used to acquire images of the flowing particles, for validation purpose. For each particle, the optical lateral position X_{opt} was computed as the distance between the particle centre and the microchannel axis. An exemplary snapshot of a flowing bead [resp. erythrocyte] is shown in Figure S3(a) [resp. (b)].

3.7 System calibration

As suggested by numerical investigation,[37] a linear mapping is used to transform the amplitude relative difference Δ into the electrical estimate X of the lateral position x:

$$X = W(\beta\Delta + \gamma), \tag{3}$$

where W is the channel width, and β and γ are calibration coefficients. In particular, β is a scaling factor depending on chip geometry, while γ takes into account possible chip asymmetries and is expected to be small. Moreover, a quadratic model can be used to obtain an electrical estimate Y of particle y-coordinate from the relative prominence P:[29]

$$Y = H(c_0 + c_1 P + c_2 P^2), \tag{4}$$

where H denotes the channel height. The parameters c_i depend on the experimental setup[38] (e.g., buffer conductivity, frequency of the AC stimulation, electrode double-layer capacitance). The parameters $\beta, \gamma, c_0, c_1, c_2$ were determined using the calibration experiment (denoted by C in Table 1) where beads can visit a large part of the channel cross-section. The calibration procedure is described in Section 5 of the ESI.

4 Results

4.1 FEM analysis of volume, shape and orientation effects

Figure 4(a)-(c) shows the simulation results relevant to an erythrocyte (volume 85.1 μm^3) flowing through the device with its axisymmetric axis aligned with x-, y- or z- channel axes (the whole set of twenty-three different orientations is reported in Figure S5). In particular, the relationship between the amplitude relative difference Δ and the erythrocyte lateral position [resp. the relationship between the relative prominence P and the erythrocyte vertical position] is reported in panel (b) [resp. (c)]. Simulation results relevant to a 7 μm diameter bead (vol-

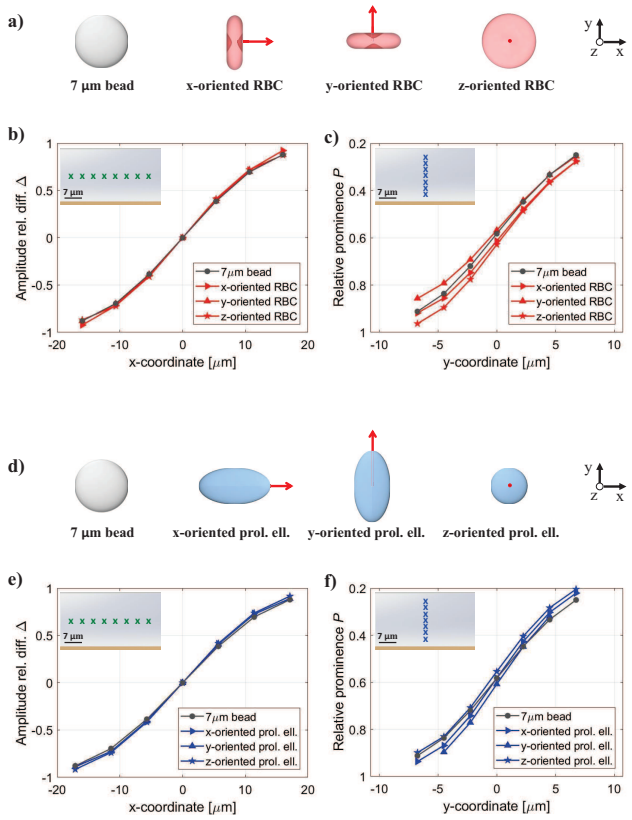

Fig. 4 (a) Schematic drawings of a 7 μm diameter bead and erythrocytes oriented along the three Cartesian axes. (b) Amplitude relative difference Δ as a function of particle lateral position (x-coordinate) and (c) relative prominence P as a function of particle vertical position (y-coordinate). The cross-sectional positions of particle center are indicated with crosses in the insets of panels (b) and (c). Panels (d), (e), and (f) are the analogous of panels (a), (b), and (c), respectively, for a prolate ellipsoid. FEM simulation results relevant to a 40 μm $\times$ 21.5 μm channel cross-section.

ume 179.6 μm^3) are also shown for comparison. The root-mean-squared difference (RMSD) across the twenty-three orientations compared to the spherical particle is 0.023 for the amplitude relative difference Δ and 0.037 for the relative prominence P. The simulation results relevant to the prolate ellipsoid (volume 113.1 μm^3, aspect ratio equal to two) are reported in Figure 4(d)-(f) and exhibit similar RMSD values (0.027 for Δ and 0.030 for P). It can be concluded that both metrics Δ and P are quite robust with respect to particle volume, shape and orientation. The proposed approach is therefore suited to spherical and non-spherical particles, and no particle orientation mechanism is required.

4.2 Experimental measurements of erythrocytes and beads

A gallery of typical experimental signals I_Δ and I_P relevant to red blood cells flowing through the device is shown in Figure 5, along with the relevant placement in the (Δ, P) plane. Fluidic settings are the same as experiment C in Table 1. The experimental traces closely mimic the simulated traces reported in Figure S2 that were relevant to 7 μm spherical beads. Recalling that biological cells behave as insulating particle at low frequency[39,40] (i.e., below the range of the β-dispersion), this result provides further evidence that the electrical metrics Δ and P are robust with respect to particle volume, shape and orientation.

A video showing examples of red blood cells and beads flowing through the chip, along with the signals I_Δ and I_P generated by their passing through, is provided as supplementary material (Video S1). For each flowing particle, the relevant values of Δ (Eq. (1)) and P (Eq. (2)) and of the corresponding electrical positions X (Eq. (3)) and Y (Eq. (4)) are also reported.

4.3 Optical validation

Electrical estimates of particle lateral positions X (Eq. (3)) were compared with the optical estimates X_{opt} (cf. Section 3.6). In the relevant experiment (denoted by V in Table 1), right and left sheath flow rates were each equal to 2.5 μl/min whereas sample flow rate was equal to 15 μl/min. The density plot of X against X_{opt} shows a good agreement between the two estimates across the whole position range, for both beads (Figure 6(a), $R^2 = 0.98$, RMSD $= 1.9$ μm, which is about 4% of channel width) and erythrocytes (Figure 6(b), $R^2 = 0.95$, RMSD $= 3.1$ μm, which is about 6% of channel width). As shown in Figure S6, similar values were obtained for chicken red blood cells, that have the shape of a prolate ellipsoid. The optical validation of the electrical estimate of particle vertical position Y (Eq. (4)) has been provided in Reale et al.[29] for spherical beads and was based on a quantitative defocusing approach.[41]

4.4 Monitoring of hydrodynamic focusing

When lateral sheath flows are used, the channel cross-section available to the sample flow is reduced along the x-direction. In general, the amount of focusing depends on flow conditions, fluid properties and geometry.[42] Being able to monitor the trajectories of the flowing particles is a crucial aspect of hydrodynamic focusing.

The results of the sheath-flow focusing experiments are shown

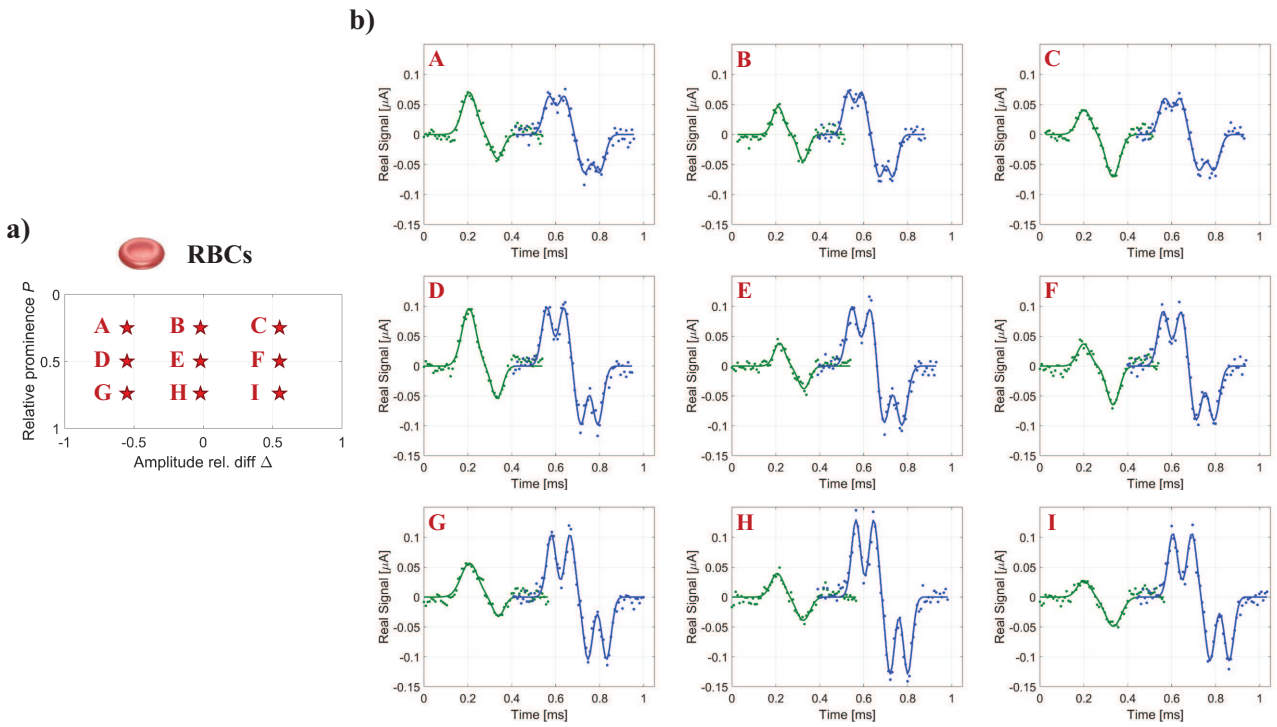

Fig. 5 Gallery of experimental signals relevant to erythrocytes with exemplary values of the (Δ, P) pair (red stars in panel (a), labeled from A to I). The real part of the corresponding differential currents I_Δ and I_P are shown in (b), respectively in green and blue (dots represent experimental points, continuous lines represent the fitted templates). For example, the erythrocyte labeled as A [resp. I] is characterized by negative Δ and low P [resp. positive Δ and high P]. Accordingly, it is flowing in the top-left [resp. bottom-right] portion of the cross-section (i.e., $x < 0$ and $y > 0$ [resp. $x > 0$ and $y < 0$]).

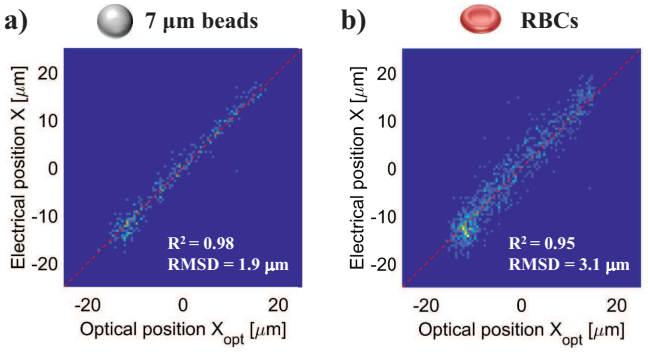

Fig. 6 Comparison between optical estimate X_{opt} and electrical estimate X of lateral positions of: a) beads (∼300 events), and b) red blood cells (∼850 events). In each density plot the bisector line is dashed in red. The regression coefficient and the root-mean-squared difference RMSD are also reported.

in Figure 7. The four experimental conditions HF-1 to HF-4 (cf. Table 1) are schematically represented in panels (a)-(d). The corresponding density plots of the electrical position Y against the electrical position X are visualized in panels (e)-(h) for the beads, and panels (i)-(l) for the erythrocytes. The 95% percentile value of the electrical lateral position, X_{H}, is indicated in experiments HF-1 to HF-3. The 2.5% and 97.5% percentile values, X_{L} and X_{H} respectively, are indicated in experiment HF-4. The values of X_{L} and X_{H} are collected in Table 2.

As expected, in the experiments HF-1 and HF-2 the beads and the erythrocytes visit a large portion of the channel cross-section, whereas in the experiments HF-3 and HF-4 they are focused in a narrow region near the channel wall or in the middle of the channel, respectively. In the central focusing experiment (HF-4), the mean value of X_{L} and X_{H} is 0.8 μm for the beads and 0.7 μm for the erythrocytes. This small off-set with respect to the value $X = 0$ is probably caused by a slight unbalance between the fluidic resistances of the right and left sheath flows. Gravitational sedimentation in the tubing may cause particle focusing in the bottom or top half of the channel (Figure 7(k) and (l)), depending on the steering angle of the tubing [43].

Additional experimental results, relevant to chicken red blood cells, are shown in Figure S7.

Finally, if also longitudinal (i.e., along z-coordinate) position sensing is required, a modified version of the approach recently proposed by Brazey et al. [27] can be implemented, under central focusing condition (cf. Section 8 of the ESI).

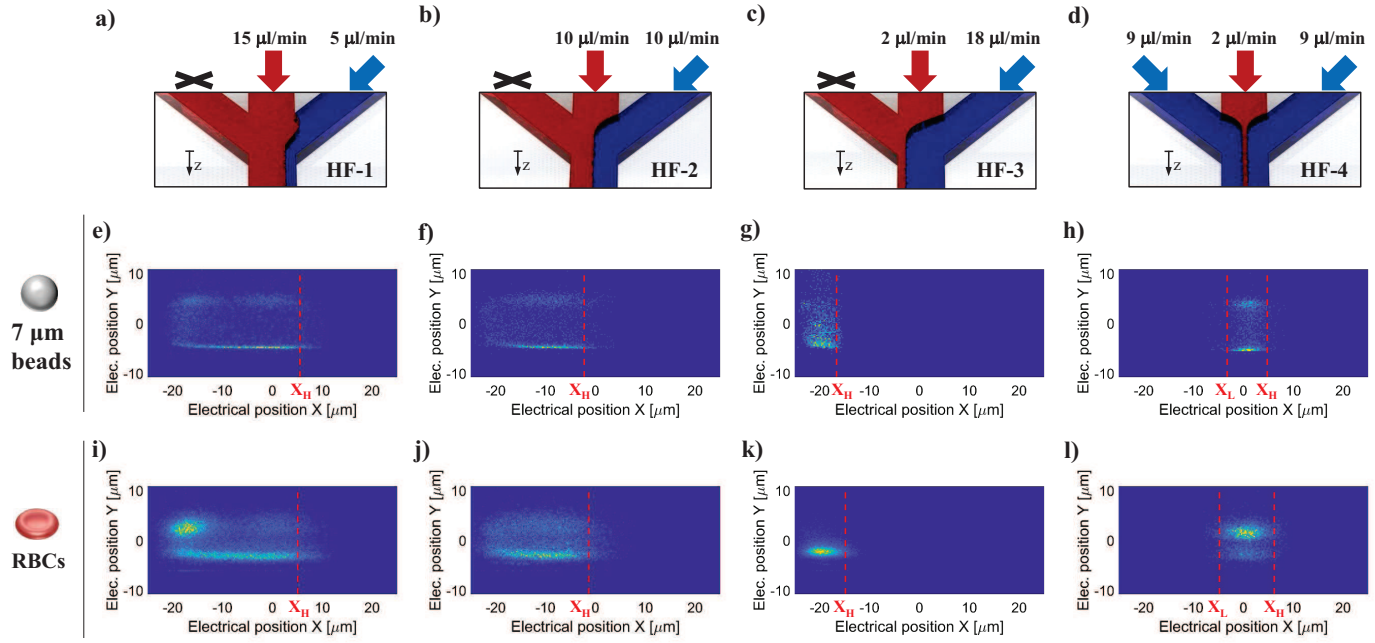

Fig. 7 Red blood cells and beads hydrodynamic focusing using sheath flows. (a)-(d) Schematic drawing of the experimental conditions HF-1 to HF-4 (cf. Table 1). (e)-(h) [resp. (i)-(l)] Density plots of the electrical cross-sectional positions (X,Y) of the beads (>2000 events in each plot) [resp. of the erythrocytes (>5000 events in each plot)]. The 95% percentile value of the electrical lateral position, X_{H}, is indicated in experiments HF-1 to HF-3. The 2.5% and 97.5% percentile values, X_{L} and X_{H} respectively, are indicated in experiment HF-4 (cf. Table 2).

Table 2 Values of the percentiles of the electrical position X relevant to the hydrodynamic focusing experiments HF-1 to HF-4 (cf. Figure 7).

Exp.	Beads X_{L} [μm]	Beads X_{H} [μm]	RBCs X_{L} [μm]	RBCs X_{H} [μm]
HF-1	–	5.5	–	5.0
HF-2	–	−2.3	–	−1.3
HF-3	–	−16.6	–	−14.8
HF-4	−3.2	4.8	−4.8	6.2

4.5 Multiparametric impedance-based characterization

Besides cross-sectional position detection, the proposed system also provides multi-parametric information useful for characterization of particle motion and electrical phenotyping of cells. An example is reported in Figure 8. The dataset is relevant to the experiment denoted by M in Table 1 where particles (erythrocytes and beads) visit a large part of the channel cross-section.

The average particle throughput (125 events/s) is reasonably stable during the 200 s of experiment duration (inset of Figure 8(a)). The empirical distribution of particle inter-arrival times is well fitted by an exponential distribution (with mean μ=8 ms and rate $\lambda = 1/\mu$=125 s^{-1}), as expected when particle occurrence is a Poisson process[44] (Figure 8(a)). Inter-arrival time statistics is useful e.g. to monitor the onset of particle trains, which have several microfluidic applications.[45]

An electrical estimate V of particle velocity is obtained from the signal $\mathrm{I_P}$ as follows:

$$V = L/\delta\,, \tag{5}$$

where L is the distance between the centres of the floating electrodes ($L = 80$ μm) and δ is the relevant transit time. A 3D scatter plot of electrical X, electrical Y and electrical V is reported in Figure 8(b) for the beads, along with the theoretical fluid velocity profile (i.e., the velocity distribution in steady state, hydrodynamically fully developed, laminar flow for Newtonian fluids in rectangular channels[46]). A good agreement is found (RMSD=0.03 m/s, that is 5% of maximum velocity).

Exploiting the amplitude of the signal $\mathrm{I_P}$ at 615 kHz and its relative prominence P, an electrical estimate of particle volume is obtained that is not affected by position-induced blurring[30] (cf. Figure S9). In particular, compensating for positional dependence, the coefficient of variation (CV) of estimated bead volume is reduced from 29.5% to 4.3%, which compares well with the manufacturer quoted value (5.1%). The histograms of the electrical volume of the erythrocytes and of the beads are shown in Figure 8(c). The red blood cell distribution width (RDW) and mean corpuscular volume (MCV), which are biomarkers with multiple clinical applications,[47] are also reported (RDW=12.7%, MCV=90 fl). By comparison, the values provided by a clinical hematology analyzer were 12.7% and 92 fl, respectively.

The ratio of the electrical volume at 1 MHz and the electrical volume at 615 kHz provides a measure of particle opacity[48] (Figure 8(d)). It is lower for the erythrocytes than for the beads, which is consistent with the capacitive behaviour of an intact cell membrane.[49,50]

5 Discussion

Microfluidic impedance cytometry is a simple electrical method for counting, identifying and monitoring cells and cellular functions at the single-cell level, with applications in basic research and diagnostics.[49] Compared with traditional approaches like

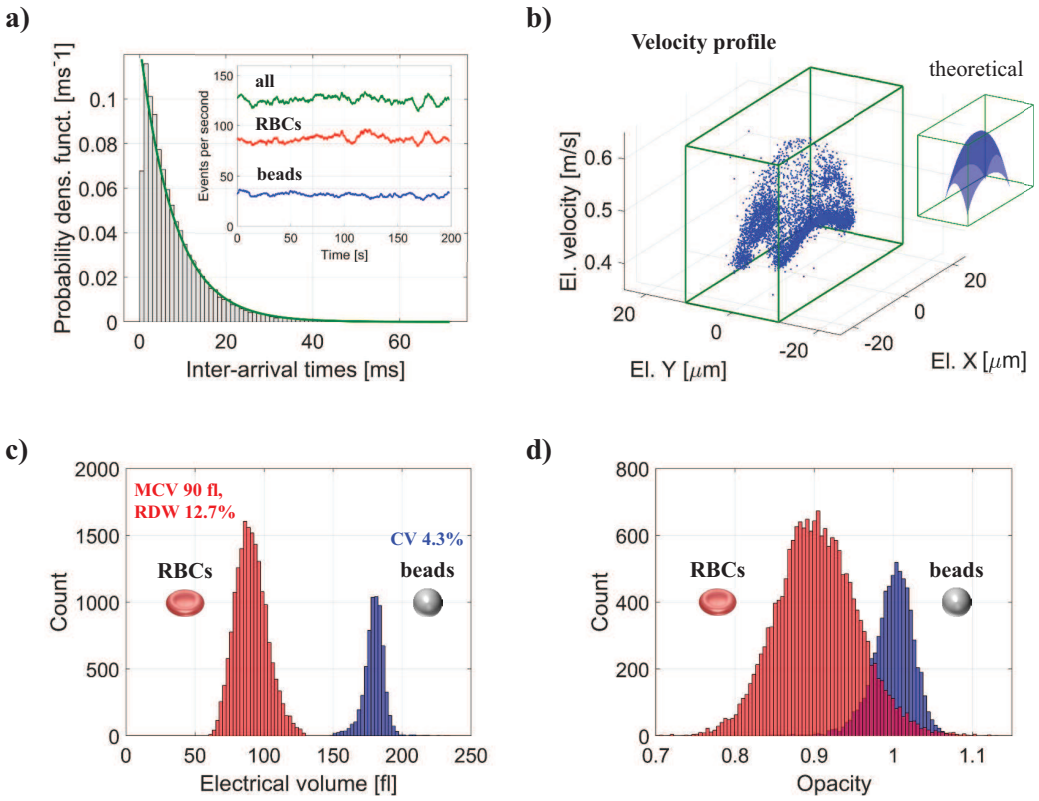

Fig. 8 Multiparametric impedance-based characterization. (a) Empirical (gray bins) and fitted (green line) probability density function of particle inter-arrival times. In the inset, particle throughput as a function of time. (b) 3D scatter plot of electrical X, electrical Y and electrical velocity V of the beads along with theoretical fluid velocity profile. (c) Histograms of electrical volume and (d) histogram of electrical opacity (in red and blue for erythrocytes and beads, respectively).

flow cytometry, its main advantages are the label-free nature, requiring minimal sample processing, and the potential for low-cost and portable implementation.[50] Whereas microfluidic impedance cytometry has been widely used for single-cell electrical characterization, its use for single-cell electrical position detection is recently emerging.[26–29]

In this work, we demonstrated an all-in-one impedance-based device for cell position detection and characterization. The features of the proposed system are summarized in Table S4 and compared with those of other relevant systems available in the literature. Our approach is suited to particles and cells, with either spherical or non-spherical geometry. To the best of our knowledge, position detection of biological cells based on a microfluidic impedance chip has not been previously reported.

Whereas most of the systems presented so far demonstrated particle position detection along one direction (channel width[26,28] or channel length[27]), cross-sectional position detection is addressed in this work. Compared to the approach in Reale et al.[29], a different strategy is used here for lateral position detection, enabling a significant reduction of the length of the relevant sensing zone (120 μm instead of 300 μm), and requiring one current signal instead of two. An accuracy in the order of 6% of channel dimension was obtained for red blood cells. By comparison, a similar accuracy was reported by Reale et al.[29] for 6 μm polystyrene beads, whereas in Wang et al.[26] (6 and 11 μm beads) and Solsona et al.[28] (83 μm beads) the accuracy was in the order of 20% and 12.5% of channel dimension, respectively. The estimation of particle cross-sectional positions along with particle velocities enabled the reconstruction of the velocity profile, that compared well with the theoretical fluid velocity profile (RMSD $= 5\%$ of maximum velocity).

The device was simultaneously used for single-cell electrical characterization in terms of size and electrical opacity. The estimation of particle position represents a significant benefit for particle/cell electrical characterization, because it allows to remove position-induced blurring from the measured particle properties. In particular, a CV of estimated bead volume of 4.3% was obtained in the characterization experiment (M), where particles visit a large portion of the channel cross-section. Similar values were reported by other groups using impedance in combination with external force fields to position particles along specific trajectories (cf. Grenvall et al.[51] and the references therein).

The demonstrated detection rate (125-460 events/s, according to flow rate) and the number of analyzed particles/cells (>2000) compares well with those of the other systems. The throughput could be further increased by increasing the flow rate (consistent with the readout rate of the electronics) or the sample concentration (at the expense of a higher fraction of coincidences[52]).

The performance assessment discussed above suggests a number of potential application scenarios for the proposed device. It could be an effective tool for studying microscale particle motion, for microfluidic sorting and separation applications, and for design and optimization of particle focusing systems. As an example, the proposed approach could be used to investigate viscoelastic cell and particle focusing.[53,54] The system, providing accurate cell sizing, is also suited to applications where cell size is a biomarker of underlying cellular processes. Examples include monitoring RDW levels for early detection of cardiovascular and cerebrovascular diseases,[55] as well as monitoring apoptotic cell death,[56] formation of cell aggregates,[57] and leucocyte activation or monocyte differentiation.[58] Moreover, the device is simple from the microfabrication point of view, because it is based on a coplanar-electrode layout, and it is easy to operate, because no focusing mechanisms are required. Therefore, when coupled with a fully integrated electronics,[59,60] it has the potential for point-of-care testing applications.

6 Conclusions

A novel strategy for the high-throughput measurement of cross-sectional positions of individual particles and cells flowing in a rectangular microchannel was presented. An all-electrical approach was implemented, based on two differential current signals whose features encode particle lateral and vertical position, respectively. The applicability of this system to cells with non-spherical morphologies was predicted in simulation and experimentally demonstrated by monitoring the hydrodynamic focusing of single erythrocytes under different sheath flow conditions. Moreover, the device was simultaneously used to measure beads/erythrocytes occurrence time, velocity, size and electrical opacity.

Acknowledgements

This work was supported by the "Scientific Independence of Young Researchers Programme" (SIR 2014) under Grant RBSI14TX20-MUSIC and by the "Mission Sustainability Programme" of the University of Rome Tor Vergata under Grant E81I18000540005-SPY.

References

1 H. Yun, K. Kim and W. G. Lee, *Biofabrication*, 2013, **5**, 022001.
2 J. Zhou and I. Papautsky, *Lab Chip*, 2013, **13**, 1121–1132.
3 J. Kim, J. Erath, A. Rodriguez and C. Yang, *Lab Chip*, 2014, **14**, 2480–2490.
4 I.-F. Cheng, V. E. Froude, Y. Zhu, H.-C. Chang and H.-C. Chang, *Lab Chip*, 2009, **9**, 3193–3201.
5 J. Gao, M. L. Y. Sin, T. Liu, V. Gau, J. C. Liao and P. K. Wong, *Lab Chip*, 2011, **11**, 1770–1775.
6 N. Piacentini, G. Mernier, R. Tornay and P. Renaud, *Biomicrofluidics*, 2011, **5**, 034122.
7 F. Shen, H. Hwang, Y. K. Hahn and J.-K. Park, *Analytical Chemistry*, 2012, **84**, 3075–3081.
8 M. Antfolk, C. Magnusson, P. Augustsson, H. Lilja and T. Laurell, *Analytical Chemistry*, 2015, **87**, 9322–9328.
9 F. Petersson, L. Åberg, A.-M. Swärd-Nilsson and T. Laurell, *Analytical Chemistry*, 2007, **79**, 5117–5123.
10 D. Holmes, G. Whyte, J. Bailey, N. Vergara-Irigaray, A. Ekpenyong, J. Guck and T. Duke, *Interface Focus*, 2014, **4**, 20140011.
11 K. K. Zeming, S. Ranjan and Y. Zhang, *Nature Communications*, 2013, **4**, 1625.

12 S. C. Hur, S.-E. Choi, S. Kwon and D. D. Carlo, *Applied Physics Letters*, 2011, **99**, 044101.

13 M. Masaeli, E. Sollier, H. Amini, W. Mao, K. Camacho, N. Doshi, S. Mitragotri, A. Alexeev and D. Di Carlo, *Phys. Rev. X*, 2012, **2**, 031017.

14 T. Roth, L. Sprenger, S. Odenbach and U. O. Häfeli, *Physics of Fluids*, 2018, **30**, 045102.

15 M. Song, Y. Lei and H. Sun, *Microsystem Technologies*, 2015, **21**, 381–391.

16 Z. Zhu, X. Xu, L. Fang, D. Pan and Q. Huang, *Sensors and Actuators B: Chemical*, 2016, **235**, 515–524.

17 B. de Wagenaar, S. Dekker, H. L. de Boer, J. G. Bomer, W. Olthuis, A. van den Berg and L. I. Segerink, *Lab Chip*, 2016, **16**, 1514–1522.

18 S. Ranjan, K. K. Zeming, R. Jureen, D. Fisher and Y. Zhang, *Lab Chip*, 2014, **14**, 4250–4262.

19 J. M. Martel, K. C. Smith, M. Dlamini, K. Pletcher, J. Yang, M. Karabacak, D. A. Haber, R. Kapur and M. Toner, *Scientific Reports*, 2015, **5**, 11300.

20 S. J. Lee and S. Kim, *Microfluidics and Nanofluidics*, 2009, **6**, 577–588.

21 C. Cierpka and C. J. Kähler, *J. Vis.*, 2012, **15**, 1–31.

22 C.-H. Lin and S.-Y. Su, *Biomicrofluidics*, 2016, **10**, 011904.

23 S. J. Williams, C. Park and S. T. Wereley, *Microfluidics and Nanofluidics*, 2010, **8**, 709–726.

24 M. H. Winer, A. Ahmadi and K. C. Cheung, *Lab Chip*, 2014, **14**, 1443–1451.

25 B. Tasadduq, G. Wang, M. E. Banani, W. Mao, W. Lam, A. Alexeev and T. Sulchek, *Flow Measurement and Instrumentation*, 2015, **45**, 218–224.

26 H. Wang, N. Sobahi and A. Han, *Lab Chip*, 2017, **17**, 1264–1269.

27 B. Brazey, J. Cottet, A. Bolopion, H. Van Lintel, P. Renaud and M. Gauthier, *Lab Chip*, 2018, **18**, 818–831.

28 M. Solsona, E. Y. Westerbeek, J. G. Bomer, W. Olthuis and A. van den Berg, *Lab Chip*, 2019, 1054–1059.

29 R. Reale, A. De Ninno, L. Businaro, P. Bisegna and F. Caselli, *Microfluidics and Nanofluidics*, 2018, **22**, 41.

30 A. De Ninno, V. Errico, F. R. Bertani, L. Businaro, P. Bisegna and F. Caselli, *Lab Chip*, 2017, **17**, 1158–1166.

31 F. Caselli, A. De Ninno, R. Reale, L. Businaro and P. Bisegna, *Sensors and Actuators B: Chemical*, 2018, **256**, 580–589.

32 R. Reale, A. De Ninno, L. Businaro, P. Bisegna and F. Caselli, *Electrophoresis*, 2019.

33 F. Caselli, P. Bisegna and F. Maceri, *J. Microelectromech. Syst.*, 2010, **19**, 1029–1040.

34 F. Caselli, M. Shaker, L. Colella, P. Renaud and P. Bisegna, *J. Microelectromech. Syst.*, 2014, **23**, 785–794.

35 S. Muñoz San Martín, J. L. Sebastián, M. Sancho and G. Álvarez, *Bioelectromagnetics*, 2006, **27**, 521–527.

36 F. Caselli and P. Bisegna, *IEEE Trans Biomed Eng*, 2016, **63**, 415–422.

37 F. Caselli, R. Reale, N. A. Nodargi and P. Bisegna, *Micromachines*, 2017, **8**, 283.

38 F. Caselli and P. Bisegna, *Med Eng Phys*, 2017, **48**, 81–89.

39 G. Schade-Kampmann, A. Huwiler, M. Hebeisen, T. Hessler and M. Di Berardino, *Cell Proliferation*, 2008, **41**, 830–840.

40 N. Haandbaek, S. C. Burgel, F. Heer and A. Hierlemann, *Lab Chip*, 2014, **14**, 369–377.

41 M. Wu, J. W. Roberts and M. Buckley, *Experiments in Fluids*, 2005, **38**, 461–465.

42 S. Tripathi, P. Chakravarty and A. Agrawal, *Current Science*, 2014, **107**, 1260–1274.

43 T. Luo, L. Fan, Y. Zeng, Y. Liu, S. Chen, Q. Tan, R. H. W. Lam and D. Sun, *Lab Chip*, 2018, **18**, 1521–1532.

44 U. Hassan and R. Bashir, *Biomedical Microdevices*, 2014, **16**, 697–704.

45 F. Del Giudice, G. D'Avino, F. Greco, P. L. Maffettone and A. Q. Shen, *Phys. Rev. Applied*, 2018, **10**, 064058.

46 M. Spiga and G. L. Morini, *Int Commun Heat Mass*, 1994, **21**, 469–475.

47 G. L. Salvagno, F. Sanchis-Gomar, A. Picanza and G. Lippi, *Critical Reviews in Clinical Laboratory Sciences*, 2015, **52**, 86–105.

48 S. Gawad, K. Cheung, U. Seger, A. Bertsch and P. Renaud, *Lab Chip*, 2004, **4**, 241–251.

49 T. Sun and H. Morgan, *Microfluid. Nanofluid.*, 2010, **8**, 423–443.

50 C. Petchakup, K. H. H. Li and H. W. Hou, *Micromachines*, 2017, **8**, 87.

51 C. Grenvall, C. Antfolk, C. Bisgaard and T. Laurell, *Lab Chip*, 2014, **14**, 4629–4637.

52 U. Hassan and R. Bashir, *Lab Chip*, 2014, **14**, 4370–4381.

53 D. Yuan, Q. Zhao, S. Yan, S.-Y. Tang, G. Alici, J. Zhang and W. Li, *Lab Chip*, 2018, **18**, 551–567.

54 M. Serhatlioglu, M. Asghari, M. Tahsin Guler and C. Elbuken, *Electrophoresis*, 2019, **40**, 906–913.

55 N. Li, H. Zhou and Q. Tang, *Disease Markers*, 2017, **2017**, 1–23.

56 D. Wlodkowic, J. Skommer and Z. Darzynkiewicz, *Cytometry Part A*, 2010, **77A**, 591–606.

57 J. Cottet, A. Kehren, S. Lasli, H. van Lintel, F. Buret, M. Frénéa-Robin and P. Renaud, *Electrophoresis*, 2019.

58 C. Petchakup, H. M. Tay, W. H. Yeap, R. Dalan, S. C. Wong, K. H. H. Li and H. W. Hou, *Biosensors and Bioelectronics*, 2018, **118**, 195–203.

59 M. Carminati, G. Ferrari, M. D. Vahey, J. Voldman and M. Sampietro, *IEEE Transactions on Biomedical Circuits and Systems*, 2017, **11**, 1438–1449.

60 A. Furniturewalla, M. Chan, J. Sui, K. Ahuja and M. Javanmard, *Microsystems Nanoengineering*, 2018, **4**, 20.